Title: Characterization of Perfluorocarbon Relaxation Times and their Influence on the Optimization of Fluorine-19 MRI at 3 Tesla
Authors: Colotti R, Bastiaansen JA, Wilson A, Flögel U, Gonzales C, Schwitter J, Stuber M, van Heeswijk RB
Journal: Magnetic Resonance in Medicine
Year: 2016
Volume:
Issue:
Pages:
DOI: 10.1002/mrm.26317

Characterization of Perfluorocarbon Relaxation Times and their Influence on the Optimization of Fluorine-19 MRI at 3 Tesla

Roberto Colotti[1], MSc, Jessica A.M. Bastiaansen[1], PhD, Anne Wilson[2], PhD, Ulrich Flögel[3], PhD, Christine Gonzales[4], PhD, Juerg Schwitter[4], MD, Matthias Stuber[1,5], PhD, Ruud B. van Heeswijk[1], PhD

[1]Department of Radiology, University Hospital (CHUV) and University of Lausanne (UNIL), Lausanne, Switzerland

[2]Ludwig Center for Cancer Research, University of Lausanne (UNIL), Epalinges, Switzerland

[3]Department of Cardiovascular Physiology, Heinrich Heine University, Düsseldorf, Germany

[4]Division of Cardiology and Cardiac MR Center, Department of Internal Medicine, University Hospital of Lausanne (CHUV), Lausanne, Switzerland

[5]Center for Biomedical Imaging (CIBM), Lausanne and Geneva, Switzerland

Address correspondence to Ruud B. van Heeswijk, PhD, CardioVascular MR Center, Centre Hospitalier Universitaire Vaudois (CHUV), Rue de Bugnon 46, BH 8.84, 1011 Lausanne, Switzerland, email: ruud.mri@gmail.com

Running Title Fluorine-19 MRI Optimization at 3 Tesla

Word Count ~4500

ABSTRACT

Purpose: To characterize and optimize ^{19}F MRI for different perfluorocarbons (PFCs) at 3 T and to quantify the loss of acquisition efficiency as a function of different temperature and cellular conditions.

Methods: T_1 and T_2 relaxation times of the commonly used PFCs perfluoropolyether (PFPE), perfluoro-15-crown-5-ether (PFCE), and perfluorooctyl bromide (PFOB) were measured in phantoms and in several different conditions (cell types, presence of fixation agent, and temperatures). These relaxation times were used to optimize pulse sequences through numerical simulations. The acquisition efficiency in each cellular condition was then determined as the ratio of the signal after optimization with the reference relaxation times and after optimization with its proper relaxation times. Finally, PFC detection limits were determined.

Results: The loss of acquisition efficiency due to parameter settings optimized for the wrong temperature and cellular condition was limited to 13%. The detection limits of all PFCs were lower at 24°C than at 37°C, and varied from 11.8±3.0 mM for PFCE at 24°C to 379.9±51.8 mM for PFOB at 37°C.

Conclusion: Optimizing ^{19}F pulse sequences with a known phantom only leads to moderate loss in acquisition efficiency in cellular conditions that might be encountered in in vivo and in vitro experiments.

Key Words: fluorine MRI, turbo spin echo, balanced steady-state free precession, perfluorocarbon, pulse sequence optimization, detection limit

INTRODUCTION

Fluorine-19 (^{19}F) MRI of perfluorocarbon (PFC) emulsions has increasingly been used in studies of inflammation due to its high specificity and chemical inertness (1,2). The lack of natural ^{19}F MR signal in the human body makes fluorine atoms a perfect candidate for an unambiguous biomarker without any natural background signal. For this reason, ^{19}F MRI offers the opportunity to locate and identify an injected substance with a high contrast-to-noise ratio (CNR) and specificity of the signal. Moreover, assuming constant radio frequency field strength B_1, the received MR signal is directly proportional to the amount of ^{19}F nuclei per voxel and the signal can be referenced to a known ^{19}F concentration, which gives ^{19}F MRI the potential to be directly quantitative (3). For these reasons, ^{19}F MRI of PFC emulsions has been used to image inflammation in vivo in animal models of cardiac and cerebral ischemia, myocarditis (3), atherosclerosis (4), pneumonia (5), and arthritis (6). The PFC nanoparticles are taken up by phagocytic cells and then accumulate at inflammatory loci in very high concentrations (7). Fluorescence and transmission electron microscopy have been used to confirm the intracellular colocalization of the PFC nanoparticles with phagocytic cells (8).

One of the primary translational goals of this technique includes inflammation imaging in patients in a clinical setting. The main technical challenge of ^{19}F MRI at lower magnetic field strengths is its low signal-to-noise ratio (SNR) per unit time. To overcome this challenge, the fluorinated biomarker needs to have a high ^{19}F molarity and needs to accumulate at high concentrations in the tissue under investigation. This strategy can be implemented through the use of specifically designed perfluorocarbons (PFCs). PFCs are derived from hydrocarbons by replacing all the hydrogen atoms with fluorine atoms. These ^{19}F based contrast agents are inert and non-toxic, and some of them have been used in American Food and Drug Administration (FDA) trials as blood volume expanders (9). ^{19}F MRI of PFCs additionally needs pulse sequences that result in high SNR per unit time, and this can be accomplished by means of adequate pulse sequence choice and parameter optimization. Such optimization mainly depends on the ^{19}F relaxation times, which in the case of PFCs have been demonstrated to depend on

temperature (10), magnetic field strength (10), and the tissue oxygenation level (11,12). It therefore follows that the optimal ^{19}F pulse sequence parameters will also change with the cellular environment of the used PFC. However, the T_1 and T_2 relaxation times cannot be quantified in each tissue and cell type before each scan, and approximate values from a well characterized phantom have to be assumed. Since the relaxation times of PFCs are significantly influenced by their direct cellular environment, the degree of signal loss caused by incorrectly optimizing pulse sequences by assuming relaxation times of a reference phantom instead of the cellular conditions of interest should be established. This signal loss in an environment due to “inaccurate” optimization is named the acquisition efficiency η in this study. It is defined as the ratio of the simulated signal after optimization with reference phantom relaxation times and the simulated signal after optimization with the actual relaxation times in that environment.

In particular, in-vitro bone-marrow-derived macrophages (13,14), ex-vivo livers (7,15), and fixed ex-vivo spleen cells suspensions (15,16) were studied, since these three groups represent the most common environments in which PFCs are imaged (without the confounding factors and variability that in-vivo studies would add). Macrophages are crucially important for ^{19}F MRI of inflammation, since they phagocytize the majority of the injected PFC nanoparticles at inflammation sites (16). Similarly, right after injection, a large part of the circulating PFC particles are phagocytized by the reticuloendothelial system, in particular liver and spleen (7). This will often result in the highest overall signal intensity in the body in these two organs, which renders them a common test and optimization target for ^{19}F MRI. Finally, since ex-vivo NMR analysis (16) can be performed on fixed PFC-loaded cell samples in order to analyze the PFC biodistribution, formaldehyde-fixed cell suspensions from spleen were analyzed as well.

Several PFCs with different characteristics have been used for inflammation imaging. In this study, the commonly used PFCs perfluoropolyether (PFPE), perfluoro-15-crown-5-ether (PFCE), and perfluorooctyl bromide (PFOB) have been investigated. PFPE is a relatively new MRI biomarker, has a linear structure with nearly magnetically equivalent ^{19}F atoms that results in a single large peak at clinical field strength, and has been used

in several preclinical inflammation studies (17,18) as well as in an FDA Phase I clinical trial for stage-4 colorectal cancer treatment (19). The second PFC of interest, PFCE, is characterized by 20 magnetically equivalent ^{19}F atoms and therefore has a single spectroscopic peak, but it has both long relaxation times and biological retention times, which might complicate its translation to the clinical setting (15). The third PFC, PFOB, has already been used as oxygen carrier (20) and blood volume expander in clinical trials (9), but it exhibits a complex spectrum with several resonances (15), which makes MRI more challenging.

In order to characterize and compare these three different PFCs, it is necessary to determine their relaxation times and their detection limits as a function of acquisition time, voxel size, and pulse sequence. This detection limit should be determined after the sensitivity of the pulse sequence is optimized by adapting the pulse sequence parameters as a function of the relaxation times. In this study we investigated two of the most commonly used ^{19}F MRI pulse sequences, i.e. the turbo spin echo (TSE) and the balanced steady state free precession (bSSFP).

The goals of this study were therefore: (I) to determine the ^{19}F relaxation times at 3 T for several commonly used PFCs at different temperature and cellular conditions; (II) to characterize the impact of changes in relaxation times of a given PFC to demonstrate the effect of different temperature and cellular conditions on the optimization of the TSE pulse sequence; (III) to evaluate and compare the detection limit for the three PFCs using both the TSE and bSSFP pulse sequences.

METHODS

Phantom Construction

Three PFC emulsions were evaluated in this study. PFPE was purchased from Celsense Inc (Pittsburgh, PA) at a ^{19}F concentration of 4.20 M (and thus a PFC concentration of 0.09 M), while PFCE and PFOB emulsions were prepared as previously described (15) at ^{19}F concentration of 3.79 M (PFC concentration of 0.19 M) and 23.85 M (PFC concentration of 1.40 M), respectively. For each PFC emulsion, a

dilution series phantom was constructed in order to establish the detection limits. Five 1 mL syringes with 2% w/v agar gel and PFC at different concentrations were placed inside a 50 mL tube with 2% w/v agar gel and no PFC. For the first syringe, the original emulsion was diluted by a factor of 4 to accommodate the agar gel that mimics the solidity of a tissue, after which it was diluted twice each time for the subsequent syringes to cover a broad range of concentrations. The last syringe in all the phantoms served as a control and did not contain any PFC.

Sample Preparation

In order to test to what degree the cellular and temperature conditions of a PFC influence its acquisition efficiency, several different PFPE cell samples were prepared from mouse-derived cells. All animal studies were approved by the local animal ethics committee. For in-vitro samples (i.e. the “in-vitro cellular condition”), bone-marrow-derived macrophages (BMM) were isolated from 8-week-old female BALB/c mouse femurs and tibiae and incubated with 10 mg/ml PFPE for 18 h for in-vitro labeling. After washing three times in PBS, the cells were separated in two samples of 2.3×10^6 and 3×10^6 cells each, and were collected in 2 ml tubes. For ex-vivo samples (i.e. the “ex-vivo cellular condition”), five 10-week-old female BALB/c mice were intravenously injected with 4×10^6 PFPE-labeled BMM 3 days prior to euthanasia, after which their livers were collected and stored for 2 years at 4°C to investigate the stability of the ^{19}F relaxation times over time. To test the effect of formaldehyde fixation on the PFPE relaxation times (i.e. the “fixed ex-vivo cellular condition”), four 8-week-old male/female ApoE-knockout mice were intravenously injected two times with 250 µL of PFPE. The animals were euthanized 2 days later, after which their spleen was excised, crushed through a 40 µM cell strainer and re-suspended in Dulbecco's Modified Eagle Medium (DMEM) containing 3% fetal calf serum (FCS). After centrifugation at 550 g, the cell pellets were re-suspended in 1% paraformaldehyde (PFA) in phosphate buffered saline (PBS) and incubated for 10 minutes at room temperature. After washing in PBS the cells were re-suspended to 10 million per mL in PBS.

Measurement of PFC ^{19}F Relaxation Times

All MR experiments were performed on a 3 T clinical scanner (Magnetom Prisma, Siemens, Erlangen, Germany) with a maximum gradient strength of 80 mT/m. A 35-mm-diameter transmit/receive birdcage radiofrequency $^{19}F/^{1}H$ (RF) coil (Rapid Biomedical, Rimpar, Germany) was used. MR measurements were performed at either room temperature (24°C) or at body temperature (37°C). In order to monitor the temperature of the samples, a thermistor probe (SA Instruments, Stony Brook, NY) was used. Tubing with circulating warm water ensured constant temperature (37 ± 1°C). For all PFC agar phantoms, the relaxation times T_1 and T_2 and the T_2/T_1 ratio were determined.

The relaxation times of the PFPE agar phantoms and the above-mentioned samples (in vitro, ex vivo, and fixed ex-vivo cellular conditions) were measured with unlocalized adiabatic spectroscopy. The T_1 relaxation times were determined using an inversion recovery (IR) spin echo (SE) pulse sequence with a variable inversion time (10 values of TI=11 to 4000 ms) and a TR of 5 s. Integrals of peaks fitted with a three-parameter inversion recovery were used to ascertain the T_1 value. The T_2 relaxation times were measured by means of a SE pulse sequence with a variable echo time (7 values of TE=9.3 to 1000 ms) and TR=5 s. Integrals of peaks fitted with a two-parameter exponential decay were used for T_2 determination. Adiabatic RF pulses were used in both pulse sequences. More specifically, a B_1-Insensitive Rotation RF pulse (BIR-4) (21) was used as 90° RF excitation pulse, a hyperbolic secant RF pulse (HS1) (22) was used as RF inversion pulse, and a hyperbolic tangent (tanh) (23,24) as RF refocusing pulse.

The T_1 relaxation time of the PFCE agar phantom was evaluated with the same adiabatic IR-SE pulse sequence, with TI=11 to 8000 ms and TR=10 s. The T_2 relaxation time was measured with the adiabatic SE pulse sequence with TE=19 to 2560 ms and a TR=10 s.

The spectral characteristics of PFOB were obtained by means of unlocalized spectroscopy using a large receiver bandwidth (20’000 Hz), TR=5 s and a sinc RF excitation pulse with duration of 100 µs in order to excite all the resonance frequencies.

The T_1 value of the different resonances of the PFOB agar phantom were evaluated using the adiabatic IR-SE pulse sequence with TI=11 to 8000 ms and TR=10 s. The T_2 values were measured twice: once with the above-mentioned adiabatic SE pulse sequences in order to measure the J-coupled relaxation times, and once with the same pulse sequence where all RF pulses have been replaced with Gaussian RF pulses (bandwidth=375 Hz at duration=5120 μs) to measure the non-J-coupled relaxation times. Due to the relatively small size of the phantoms compared to routine clinical shimming volumes, manual shimming was performed before each experiment in order to minimize the fluorine line width.

Numerical Simulations

In order to optimize the TSE pulse sequence, Bloch equation simulations (25) were performed in Matlab (The MathWorks, Inc, Natick, MA, USA). The signal per unit time, i.e. the signal normalized by $\sqrt{TR \times ETL \times BW}$ (26), was mapped as a function of TR, ETL, and BW for a PFC-specific set of T_1 and T_2 values as determined in the above-described experiments. These maps were used to determine the combination of TR, ETL, and BW that leads to maximum signal strength per unit time. These simulations were performed both with and without a longitudinal magnetization restoration (LMR) RF pulse of -90° after the echo train (27).

Acquisition Efficiency

To define the link between relaxation times alteration and different temperature and cellular conditions, the acquisition efficiency η for that condition was then defined as:

$$\eta_{cond} = \frac{\left[S/\sqrt{TR \times ETL \times BW}\right]_{ref}}{\left[S/\sqrt{TR \times ETL \times BW}\right]_{cond}}, \quad (1)$$

where S stands for the signal, while *ref* indicates the signal calculated at parameters obtained for the 24°C phantom (considered to be the reference) and *cond* indicates the signal calculated at parameters obtained for different relaxation times of the

temperature and cellular condition. The acquisition efficiency is expected to always be ≤1, since the choice of sub-optimal parameters will inevitably lead to a lower signal.

The simulated acquisition efficiency was experimentally verified by imaging the ex-vivo cellular condition with both the phantom reference parameters and its optimal parameters, and taking the ratio of the signal intensities normalized by $\sqrt{TR \times ETL \times BW}$. This was repeated at 24°C and 37°C, and with and without the LMR pulse.

Detection Limit Analysis

The detection limit was separately determined for both the TSE and bSSFP pulse sequences. For the TSE pulse sequence, the PFC-specific optimal TR, ETL, and BW were determined as described above. Common parameters for all TSE imaging included: TE=13 ms, field of view (FOV)=64×64 mm^2, matrix size=128×128, 128 signal averages, three slices with thickness 3 mm, 1 mm inter-slice distance, and BW=130 Hz/pixel.

Simultaneously, for the bSSFP pulse sequence, the optimal flip angle α that was used when determining the detection limit is given by (28):

$$\cos(\alpha) = \frac{T_1/T_2 - 1}{T_1/T_2 + 1} \tag{2}$$

For all the PFC phantoms, bSSFP images were acquired with the following sequence parameters: TE=5.41 ms, TR=10.82 ms, FOV=64×64 mm^2, matrix size=128×128, 128 signal averages, three slices with thickness 3 mm, 1 mm inter-slice distance, and BW=130 Hz/pixel.

The images obtained with both these optimized pulse sequences were analyzed in Matlab in order to determine the SNR of the detected tubes. Since a single-channel birdcage coil was used, the SNR of a region of interest (ROI) was calculated as the ratio between the average signal in the ROI and the standard deviation in a background ROI of at least 20 by 20 pixels outside the object of interest. For the PFOB phantom, the use of the lowest possible BW combined with the relative large chemical shifts between the

resonances (2-5 kHz) caused all chemical shift ghosts to appear well outside the phantom itself. This allowed any signal cancellation due to overlapping images from different resonances with different phases to be avoided.

A linear fit of the ^{19}F concentration versus the SNR was performed, and the minimum detectable concentration (i.e. the detection limit) was considered to be at SNR=4 (29). In order to normalize the values obtained with the two pulse sequences, the detection limit was normalized to an acquisition time of 600 s, a voxel volume of 1 mm^3, and a pixel bandwidth of 300 Hz/px, yielding:

$$Detection\ Limit = \frac{C_{min}}{V_{norm}/V_{act} \times \sqrt{t_{norm}/t_{act}} \times \sqrt{BW_{act}/BW_{norm}}} \qquad (3)$$

Where V is the volume, t is the duration of the pulse sequence, BW is the pixel bandwidth, C is the ^{19}F molar concentration, *norm* denotes the values used for normalization, and *act* represents the actual values.

Statistics

For every PFC, the detection limit was calculated for each of the three imaged slices and for both the TSE and bSSFP pulse sequences. Data are therefore presented as mean ± standard deviation over the three imaged slices. A linear least squares fitting in which each data point carries equal weight has been used for the ^{19}F concentration vs. SNR relationship, while an exponential least squares fitting was used to determine the T_1 and T_2 relaxation times. Since they are assumed to be normally distributed, the relaxation times are presented with their standard deviation.

RESULTS

Characterization of PFCs

The relaxation times of all samples have been successfully characterized to at least 10% precision (Table 1). PFPE had a significantly lower T_1 than the other compounds, while PFCE presented a high T_2/T_1 ratio. The PFOB spectrum at 3 T is characterized by five ^{19}F resonance groups (30), since the CF_2 (γ, δ-ε, ζ) multiplet was not completely resolved on the clinical system, despite manual shimming (Figure 1). The T_1 relaxation times of all resonances of PFOB were similar, while there was a large difference between their T_2 values due to J-coupling. Although RF pulses with a low bandwidth were used to selectively excite the individual peak of interest, in the case of the CF_2 (γ, δ-ε, ζ) multiplet it was not possible to suppress the J-coupling effect (Table 2).

Acquisition Efficiency

Since the relaxation times depend on temperature and cellular conditions, the optimal TR and ETL for the TSE pulse sequence change accordingly. In particular, the T_1 values of PFPE increased significantly with temperature in all conditions. The T_1 value also increased in both the ex-vivo and in-vitro cellular conditions relative to the phantom (61-86%, Figure 2a), while it increased slightly less in the fixed cells (21%). At both temperature conditions, the T_2 value stayed approximately the same in both the in-vitro and ex-vivo conditions (Figure 2b), but decreased by 40% in the fixed ex-vivo condition.

In general, for both the TSE pulse sequence with and without LMR, the lowest BW (i.e. 130 Hz/px) allowed the signal maximization and thus the highest acquisition efficiency. In particular, for the TSE pulse sequence without LMR, a small decrease in pulse sequence acquisition efficiency η was observed at 24°C for the in-vitro, ex-vivo, and fixed ex-vivo cellular environments (6.5, 3.8 and 5.0%, respectively, Figure 3b), while a slightly larger decrease in η was observed at 37°C for all the cellular environments (10.0, 12.7, and 7.7%, respectively, Figure 3b). Similar but slightly smaller efficiency decreases were observed for the TSE pulse sequence with LMR on at both 24°C and 37°C (Figure 3c).

The experimentally determined acquisition efficiencies in the ex-vivo samples showed good agreement with the simulated values based on the measured relaxation times (Figure 4). While there were differences up to 5% between the simulated and experimental acquisition efficiencies, the simulated results always fell within the standard deviation of the experimental results, and there was no consistent trend to the difference.

Detection Limits

For each PFC phantom, the relaxation times measured at both 24°C and at 37°C have been used to obtain the optimized parameters for the TSE pulse sequence with LMR off and on, and to obtain the optimal flip angle for the bSSFP pulse sequence (Table 3). The lowest available bandwidth choice consistently led to the highest signal per unit time for both pulse sequences. The pulse sequence optimization for the PFOB phantom was performed with the relaxation times of the CF_3 (θ) peak, since this peak is characterized by the highest signal strength and the highest T_2/T_1 ratio.

SNR measurements in the PFC phantoms at both 24°C and at 37°C (Figure 5) were used to obtain the optimized detection limit of both the TSE and bSSFP pulse sequences. It can be observed that when LMR was enabled, the detection limit for PFPE, PFCE, and PFOB for the TSE pulse sequence at both investigated temperatures improved (Table 4).

DISCUSSION AND CONCLUSIONS

In this study, the relaxation times of three perfluorocarbon emulsions that are commonly used in fluorine-19 MR imaging were determined at the clinical magnetic field strength of 3 T and were used to optimize the TSE and bSSFP pulse sequences. These optimized pulse sequences were then used to establish the detection limits of the PFCs and to investigate the loss of acquisition efficiency in three different conditions that represent the most common environments in which fluorine-19 MRI of PFCs is performed.

PFPE is characterized by the shortest T_1 value, which allows for more rapid pulse sequences. It has been recently used in several preclinical inflammation studies (17,18) but it needs to be further investigated to allow clinical application, since, to our knowledge, its clearance rate from the body has not been studied yet. PFCE has the highest T_2/T_1 ratio and thus is ideal for the bSSFP pulse sequence. It has a single spectroscopic peak and it has been widely used for inflammation imaging (3,4) and cell tracking (31). However, it has been demonstrated that it remains in the liver and spleen for several months after administration (15). In contrast, PFOB remains in the liver and spleen a twenty-fold shorter time (15), it has been already used in humans as oxygen carrier (20) and the PFC fraction in the emulsion has been increased from 70% w/v (15) up to 90% w/v without compromising its stability (20,32,33). From a safety point of view, it therefore might be considered the best-suited candidate for inflammation imaging in humans. However, its complex spectrum causes chemical shift artifacts and signal loss due to homonuclear J-coupling. As reported in previous studies, this technical hurdle can be overcome by the use of a bSSFP ultrashort echo-time (UTE) pulse sequence (34), the use of a multi-chemical-shift-selective (MCSS) TSE pulse sequence (35), or the use of a SE sequence with a specific bandwidth of the refocusing pulse (36).

The order of magnitude of the loss of acquisition efficiency η due to different cellular conditions was evaluated with PFPE and validated experimentally. In general, the T_1 value increased with temperature and in all cellular conditions, while the T_2 value remained mostly the same as in the phantom, except for the fixed ex-vivo samples, where T_2 was shorter due to the presence of formaldehyde (37). Fortunately the acquisition efficiency loss was moderate, and indicated that using the TSE pulse sequence with parameters optimized for a room-temperature agar-gel phantom would result in a usually acceptable signal loss in the body of less than 13% with LMR off and less than 9.5% with LMR on.

The relaxation times and the optimized parameters determined in this study were also used to ascertain the detection limit of the different PFCs for the TSE and the bSSFP pulse sequences at both 24°C and at 37°C. For all the investigated PFCs, the use of longitudinal magnetization restoration (LMR) allows for higher SNR per unit time (26)

and therefore resulted in a slightly improved trend in the detection limit for the TSE pulse sequence. On the other hand, due to the LMR activation the optimal TR was significantly lower, limiting the time available for 2D multi-slice acquisition. For PFOB, only the CF_3 (θ) resonance group was used and therefore only three out of seventeen ^{19}F nuclei were excited. As reported (34), this resulted in a significantly higher detection limit than PFPE and PFCE. In general, imaging performed at 37°C for both pulse sequences resulted in a higher detection limit, most likely due to higher T_1 relaxation times and thus lower T_2/T_1 ratios.

The relaxation times and detection limits found in this study were similar to those found by other groups for other field strengths and pulse sequences. Jacoby et al. (15) recently characterized a PFCE emulsion prepared as in this study at 9.4 T and found a similar T_2/T_1 ratio at 37°C. Mastropietro et al. (26) optimized the TSE pulse sequence for different phantoms of KPF_6 and found a KPF_6 detection limit of 0.5 mM in a water solution at 7 T. This value, when normalized as in the present study, resulted in a detection limit of 5 mM, comparable to those obtained in this study for PFCE at 3 T. Goette et al. (34) recently analyzed a PFOB phantom with a bSSFP UTE pulse sequence at 3 T (34). The T_1 and T_2 relaxation times for the CF_3 (θ) were measured and agreed with those measured in the current study. The detection limits reported here are furthermore up to several orders of magnitude below the ^{19}F tissue concentrations (~6 M) that have been previously reported (7). Finally, the detection limit of PFCE with a gradient echo (GRE) pulse sequence was determined with a small surface coil at 9.4 T (38), which resulted in a detection limit of 0.5 mM when normalized as in this study, demonstrating the increase in signal sensitivity when using a small surface coil and higher magnetic field strengths.

This study also has several limitations. The TSE pulse sequence parameters have been optimized on a theoretical basis, but the resulting acquisition efficiency was only validated in ex-vivo samples. It remains to be confirmed in the other sample types, although an experimental validation of the TSE parameter simulations was performed by Mastropietro et al. (26). The detection limit was furthermore ascertained in phantoms and remains to be investigated in vivo. However, the exact concentration in vivo will be

challenging to control, since it will depend on the animal's PFC absorption, clearance and biodistribution (i.e. species and time point after injection), while the detection limit might be overestimated due to animal motion. The RF coil used in this study (a 35-mm-diameter birdcage) cannot be used in any human studies. However, this single-element birdcage has the advantage that it allows for direct quantification, which was required for the quantitative goals of this study. Simultaneously, the most suitable RF coil in an initial human application will strongly depend on the targeted body part, so a definitive human coil could not be chosen for this study. We would suggest using an array of small and sensitive surface coils in future initial human studies. Such arrayed surface coils (as for example used for the human carotids and hands) have similar, if not higher, sensitivities as the birdcage coil used here, but would make absolute quantification more challenging. Moreover, the used resolution was adapted to the specific RF coil and the phantom size (i.e. 6-mm-diameter syringes). However, since the detection limit scales linearly with the voxel size, it should be straightforward to extrapolate the results obtained in this study to any future human applications. Finally, the specific absorption rate (SAR) has not been included as parameter in the simulation of the TSE pulse sequence, although all optimal parameter combinations were well within the SAR limits of the scanner.

The detection limits reported in this study apply for 2D pulse sequences with a fully acquired k-space and a single-element volume coil at 3 T. For future applications, by applying compressed sensing (39) or by using a more sensitive surface coil or coil array and parallel imaging, it should be possible to further improve the detection limit of the acquisition system at 3 T. Moreover, since the voxel sizes commonly used in human applications (up to 2×2×8 mm^3) are much larger than the size used here (normalized to 1×1×1 mm^3), it is reasonable to expect that a higher SNR could be obtained at similar concentrations, which may lead to an improved detection limit.

In conclusion, we have reported relaxation times of three PFCs and determined their optimized detection limits at 3 T, and demonstrated that the loss of acquisition efficiency for PFC due to parameter settings optimized for the incorrect temperature and cellular condition is moderate.

ACKNOWLEDGMENTS

This work has been supported by grants from the Swiss Heart Foundation, the Pierre Mercier Foundation, the Swiss Multiple Sclerosis Society and the Swiss National Science Foundation (PZ00P3-154719) to RBvH, a grant from the Swiss National Science Foundation (310030_144077) to JS, as well as the Centre d'Imagerie BioMédicale (CIBM) of the UNIL, UNIGE, HUG, CHUV, EPFL, and the Leenaards and Jeantet Foundations.

REFERENCES

1. Ruiz-Cabello J, Barnett BP, Bottomley PA, Bulte JW. Fluorine (19F) MRS and MRI in biomedicine. NMR Biomed 2011;24(2):114-129.
2. Flogel U, Ding Z, Hardung H, Jander S, Reichmann G, Jacoby C, Schubert R, Schrader J. In vivo monitoring of inflammation after cardiac and cerebral ischemia by fluorine magnetic resonance imaging. Circulation 2008;118(2):140-148.
3. van Heeswijk RB, De Blois J, Kania G, Gonzales C, Blyszczuk P, Stuber M, Eriksson U, Schwitter J. Selective in vivo visualization of immune-cell infiltration in a mouse model of autoimmune myocarditis by fluorine-19 cardiac magnetic resonance. Circ Cardiovasc Imaging 2013;6(2):277-284.
4. van Heeswijk RB, Pellegrin M, Flogel U, Gonzales C, Aubert JF, Mazzolai L, Schwitter J, Stuber M. Fluorine MR Imaging of Inflammation in Atherosclerotic Plaque in Vivo. Radiology 2014:141371.
5. Ebner B, Behm P, Jacoby C, Burghoff S, French BA, Schrader J, Flogel U. Early assessment of pulmonary inflammation by 19F MRI in vivo. Circ Cardiovasc Imaging 2010;3(2):202-210.
6. Flogel U, Burghoff S, van Lent PL, Temme S, Galbarz L, Ding Z, El-Tayeb A, Huels S, Bonner F, Borg N, Jacoby C, Muller CE, van den Berg WB, Schrader J. Selective activation of adenosine A2A receptors on immune cells by a CD73-dependent prodrug suppresses joint inflammation in experimental rheumatoid arthritis. Sci Transl Med 2012;4(146):146ra108.
7. Mattrey RF, Long DM, Multer F, Mitten R, Higgins CB. Perfluoroctylbromide: a reticuloendothelial-specific and tumor-imaging agent for computed tomography. Radiology 1982;145(3):755-758.
8. Ahrens ET, Flores R, Xu H, Morel PA. In vivo imaging platform for tracking immunotherapeutic cells. Nature biotechnology 2005;23(8):983-987.
9. Riess JG. Perfluorocarbon-based oxygen delivery. Artif Cells Blood Substit Immobil Biotechnol 2006;34(6):567-580.
10. Kadayakkara DK, Damodaran K, Hitchens TK, Bulte JW, Ahrens ET. (19)F spin-lattice relaxation of perfluoropolyethers: Dependence on temperature and magnetic field strength (7.0-14.1T). J Magn Reson 2014;242:18-22.
11. Duong TQ, Kim SG. In vivo MR measurements of regional arterial and venous blood volume fractions in intact rat brain. Magn Reson Med 2000;43(3):393-402.
12. Zhong J, Sakaki M, Okada H, Ahrens ET. In vivo intracellular oxygen dynamics in murine brain glioma and immunotherapeutic response of cytotoxic T cells observed by fluorine-19 magnetic resonance imaging. PLoS One 2013;8(5):e59479.
13. Temme S, Bonner F, Schrader J, Flogel U. 19F magnetic resonance imaging of endogenous macrophages in inflammation. Wiley interdisciplinary reviews Nanomedicine and nanobiotechnology 2012;4(3):329-343.
14. Kadayakkara DK, Ranganathan S, Young WB, Ahrens ET. Assaying macrophage activity in a murine model of inflammatory bowel disease using fluorine-19 MRI. Laboratory investigation; a journal of technical methods and pathology 2012;92(4):636-645.
15. Jacoby C, Temme S, Mayenfels F, Benoit N, Krafft MP, Schubert R, Schrader J, Flogel U. Probing different perfluorocarbons for in vivo inflammation imaging by 19F MRI: image reconstruction, biological half-lives and sensitivity. NMR Biomed 2014;27(3):261-271.
16. Ahrens ET, Young WB, Xu H, Pusateri LK. Rapid quantification of inflammation in tissue samples using perfluorocarbon emulsion and fluorine-19 nuclear magnetic resonance. BioTechniques 2011;50(4):229-234.

17. Vasudeva K, Andersen K, Zeyzus-Johns B, Hitchens TK, Patel SK, Balducci A, Janjic JM, Pollock JA. Imaging neuroinflammation in vivo in a neuropathic pain rat model with near-infrared fluorescence and 19F magnetic resonance. PLoS One 2014;9(2):e90589.
18. Balducci A, Helfer BM, Ahrens ET, O'Hanlon CF, 3rd, Wesa AK. Visualizing arthritic inflammation and therapeutic response by fluorine-19 magnetic resonance imaging (19F MRI). J Inflamm (Lond) 2012;9(1):24.
19. Ahrens ET, Helfer BM, O'Hanlon CF, Schirda C. Clinical cell therapy imaging using a perfluorocarbon tracer and fluorine-19 MRI. Magn Reson Med 2014;72(6):1696-1701.
20. Riess JG. Oxygen carriers ("blood substitutes")--raison d'etre, chemistry, and some physiology. Chem Rev 2001;101(9):2797-2920.
21. Staewen RS, Johnson AJ, Ross BD, Parrish T, Merkle H, Garwood M. 3-D FLASH imaging using a single surface coil and a new adiabatic pulse, BIR-4. Invest Radiol 1990;25(5):559-567.
22. Silver MS, Joseph RI, Hoult DI. Highly selective $\pi/2$ and π pulse generation. J Magn Reson 1984;59:347–351.
23. Garwood M, Ke Y. Symmetric pulses to induce arbitrary flip angles with compensation for RF inhomogeneity and resonance offsets. J Magn Reson 1991;94:511–525.
24. Hwang TL, van Zijl PC, Garwood M. Fast broadband inversion by adiabatic pulses. J Magn Reson 1998;133(1):200-203.
25. Bloch F. Nuclear Induction. Phys Rev 1946;70:460-474.
26. Mastropietro A, De Bernardi E, Breschi GL, Zucca I, Cametti M, Soffientini CD, de Curtis M, Terraneo G, Metrangolo P, Spreafico R, Resnati G, Baselli G. Optimization of rapid acquisition with relaxation enhancement (RARE) pulse sequence parameters for (1)(9)F-MRI studies. J Magn Reson Imaging 2014;40(1):162-170.
27. Tegenfeldt J, Haeberlen U. Cross polarization in solids with flip-back of I-spin magnetization. J Magn Reson Imaging 1979;36:453-457.
28. Scheffler K, Lehnhardt S. Principles and applications of balanced SSFP techniques. Eur Radiol 2003;13(11):2409-2418.
29. Watts R, Wang Y. k-space interpretation of the Rose Model: noise limitation on the detectable resolution in MRI. Magn Reson Med 2002;48(3):550-554.
30. Shukla HP, Mason RP, Woessner DE, Antich PP. A Comparison of Three Commercial Perfluorocarbon Emulsions as High-Field 19F NMR Probes of Oxygen Tension and Temperature. J Magn Reson 1995;Volume 106(Issue 2).
31. Ruiz-Cabello J, Walczak P, Kedziorek DA, Chacko VP, Schmieder AH, Wickline SA, Lanza GM, Bulte JW. In vivo "hot spot" MR imaging of neural stem cells using fluorinated nanoparticles. Magn Reson Med 2008;60(6):1506-1511.
32. Bruneton JN, Falewee MN, Francois E, Cambon P, Philip C, Riess JG, Balu-Maestro C, Rogopoulos A. Liver, spleen, and vessels: preliminary clinical results of CT with perfluorooctylbromide. Radiology 1989;170(1 Pt 1):179-183.
33. Riess JG. Overview of progress in the fluorocarbon approach to in vivo oxygen delivery. Biomater Artif Cells Immobilization Biotechnol 1992;20(2-4):183-202.
34. Goette MJ, Keupp J, Rahmer J, Lanza GM, Wickline SA, Caruthers SD. Balanced UTE-SSFP for (19) F MR imaging of complex spectra. Magn Reson Med 2015;74(2):537-543.
35. Jacoby C, Oerther T, Temme S, Schrader J, Flögel U. Simultaneous MR imaging at different resonance frequencies using multi chemical shift selective (MCSS) RARE. Proceedings of the 22nd Annual Meeting of ISMRM, Milano, Italy, 2014;Abstract 2927.
36. Giraudeau C, Flament J, Marty B, Boumezbeur F, Meriaux S, Robic C, Port M, Tsapis N, Fattal E, Giacomini E, Lethimonnier F, Le Bihan D, Valette J. A new paradigm for high-sensitivity 19F

magnetic resonance imaging of perfluorooctylbromide. Magn Reson Med 2010;63(4):1119-1124.
37. Fishbein KW, Gluzband YA, Kaku M, Ambia-Sobhan H, Shapses SA, Yamauchi M, Spencer RG. Effects of formalin fixation and collagen cross-linking on T2 and magnetization transfer in bovine nasal cartilage. Magn Reson Med 2007;57(6):1000-1011.
38. van Heeswijk RB, Pilloud Y, Flogel U, Schwitter J, Stuber M. Fluorine-19 magnetic resonance angiography of the mouse. PLoS One 2012;7(7):e42236.
39. Zhong J, Mills PH, Hitchens TK, Ahrens ET. Accelerated fluorine-19 MRI cell tracking using compressed sensing. Magn Reson Med 2013;69(6):1683-1690.

TABLES

Table 1. Relaxation times of the perfluorocarbons used in this study. Unlocalized spectroscopy was performed to characterize PFPE, PFCE, and PFOB at 24°C and 37°C. Only the CF_3 resonance of PFOB is included, since it is characterized by the highest absolute value and by the highest T_2/T_1 ratio. The PFOB T_2 relaxation time was measured through selective excitation. The relaxation time values are reported with one standard deviation.

Resonance	T_1 (ms)	T_2 (ms)	T_2/T_1 (-)
	24°C		
PFPE	423 ± 25	155 ± 12	0.36
PFCE	919 ± 31	588 ± 28	0.64
PFOB [CF_3 (θ)]	1092 ± 38	283 ± 20	0.26
	37°C		
PFPE	597 ± 40	164 ± 8	0.27
PFCE	1171 ± 30	596 ± 22	0.50
PFOB [CF_3 (θ)]	1416 ± 7	286 ± 30	0.20

Table 2. Relaxation times of the PFOB resonances at 24°C. The PFOB T_2 relaxation times were measured in phantoms at 24°C with and without selective excitation. In case of non-selective excitation, all the CF_2 resonances are characterized by short T_2 values. The CF_2 (γ, δ-ε, ζ) multiplet is the only one that is still J-coupled despite the selective excitation. The relaxation time values are reported in order of decreasing resonance frequency and with one standard deviation.

Resonance	T_1 (ms)	T_2 (ms)	
		Selective Excitation	Non-Selective Excitation
CF_2Br (α)	1142 ± 43	184 ± 8	213 ± 23
CF_3 (θ)	1092 ± 38	283 ± 20	291 ± 29
CF_2 (β)	1170 ± 30	176 ± 9	7.2 ± 0.4
CF_2 (γ,δ-ε,ζ)	1108 ± 12	10.1 ± 1.3	6.8 ± 0.5
CF_2 (η)	1180 ± 35	195 ± 14	8.0 ± 0.4

Table 3. Optimized pulse sequence parameters for PFCs at 24°C and 37°C. By means of T_1 and T_2 relaxation times measured at 24°C and 37°C, the optimized repetition time and echo train length with longitudinal magnetization restoration (LMR; a -90° "flip-back" pulse) off and on were determined for the PFCs in the TSE pulse sequence, as was the optimal bSSFP flip angle. For both pulse sequences, the pixel bandwidth was minimized to 130 Hz/px. In almost all the cases, the optimization with the LMR pulse on leads to a slightly faster pulse sequence. For comparison of these parameters, the resulting acquisition time for a single-slice image with 1 average and a 128x128 matrix has been reported for the TSE pulse sequence. Similarly, for the bSSFP pulse sequence, the acquisition time for a single-slice image with 1 average, 128x128 matrix and TR=10.82 ms has been reported.

Resonance	TSE LMR Off		TSE LMR On		TSE Acquisition Time (s)		bSSFP Flip Angle (°)	bSSFP Acquisition Time (s)
	24°C							
	TR (ms)	ETL	TR (ms)	ETL	LMR Off	LMR On		
PFPE	825	12	485	7	8.8	8.8	62°	1.4
PFCE	2075	40	795	16	6.6	6.3	77°	1.4
PFOB [$CF_3(\theta)$]	1925	22	915	11	11.2	10.6	54°	1.4
	37°C							
	TR (ms)	ETL	TR (ms)	ETL	LMR Off	LMR On		
PFPE	1075	13	585	7	10.6	10.7	55°	1.4
PFCE	2465	42	945	17	7.5	7.1	71°	1.4
PFOB [$CF_3(\theta)$]	2365	23	1095	11	13.2	12.7	48°	1.4

Table 4: PFCs Detection Limits at 3 T. The detection limit for different PFCs for optimized TSE and bSSFP pulse sequences at room temperature (24°C) and at body temperature (37°C) were determined. Despite the pulse sequence parameters being optimized for the relaxation times at 37°C, the detection limit was consistently higher when the temperature increased. The detection limit was normalized to an acquisition time of 600 s, a voxel volume of 1 mm^3 and a pixel bandwidth of 300 Hz/px. The actual acquisition times for both TSE and bSSFP pulse sequences are reported. Note that the detection limits are expressed as fluorine atom concentrations (since these relate directly to the generated signal), and not as PFC molecule concentrations, which would result in lower values.

Resonance	^{19}F pulse sequence	Detection Limit (mM ^{19}F)		Acquisition Time (s)	
		24°C	37°C	24°C	37°C
PFPE	TSE LMR off	40.8 ± 5.9	51.5 ± 12.4	1126.4	1361.1
	TSE LMR on	36.6 ± 13.3	47.0 ± 14.1	1135.2	1369.2
	bSSFP	23.5 ± 3.0	31.2 ± 4.8	177.3	177.3
PFCE	TSE LMR off	35.7 ± 6.2	42.0 ± 9.1	892.5	941.1
	TSE LMR on	27.3 ± 6.1	35.1 ± 7.2	814.1	910.7
	bSSFP	11.8 ± 3.0	21.8 ± 5.5	177.3	177.3
PFOB [CF_3 (θ)]	TSE LMR off	313.3 ± 33.0	379.9 ± 51.8	1429.9	1688.3
	TSE LMR on	287.4 ± 45.8	365.9 ± 5.5	1362.9	1638.4
	bSSFP	92.2 ± 16.1	137.8 ± 7.9	177.3	177.3

FIGURE LEGEND

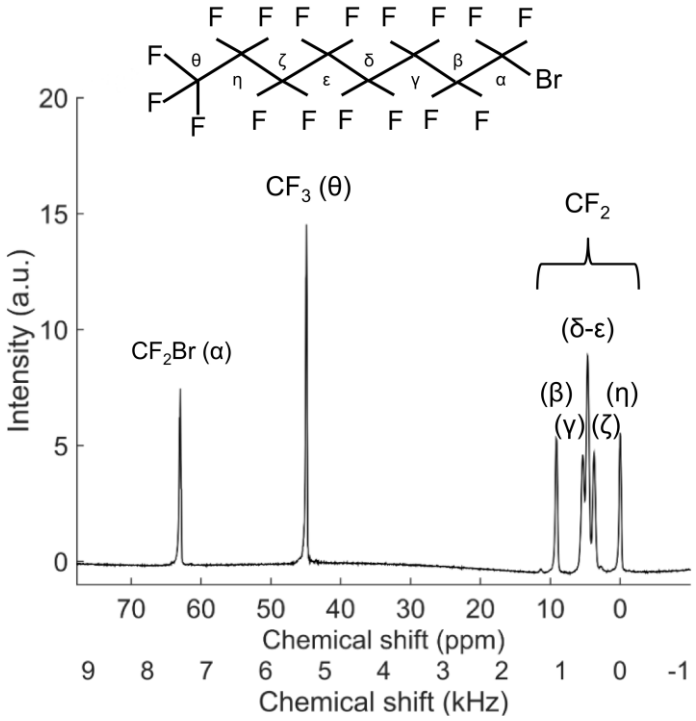

Figure 1: The molecular structure and MR spectrum of perfluoro octylbromide at 3 T. Two separate resonances can be observed (CF_2Br (α) and CF_3 (θ)) in addition to the J-coupled CF_2 spectral group with five distinct spectral components. The horizontal axis was zeroed on the peak with the lowest resonance frequency.

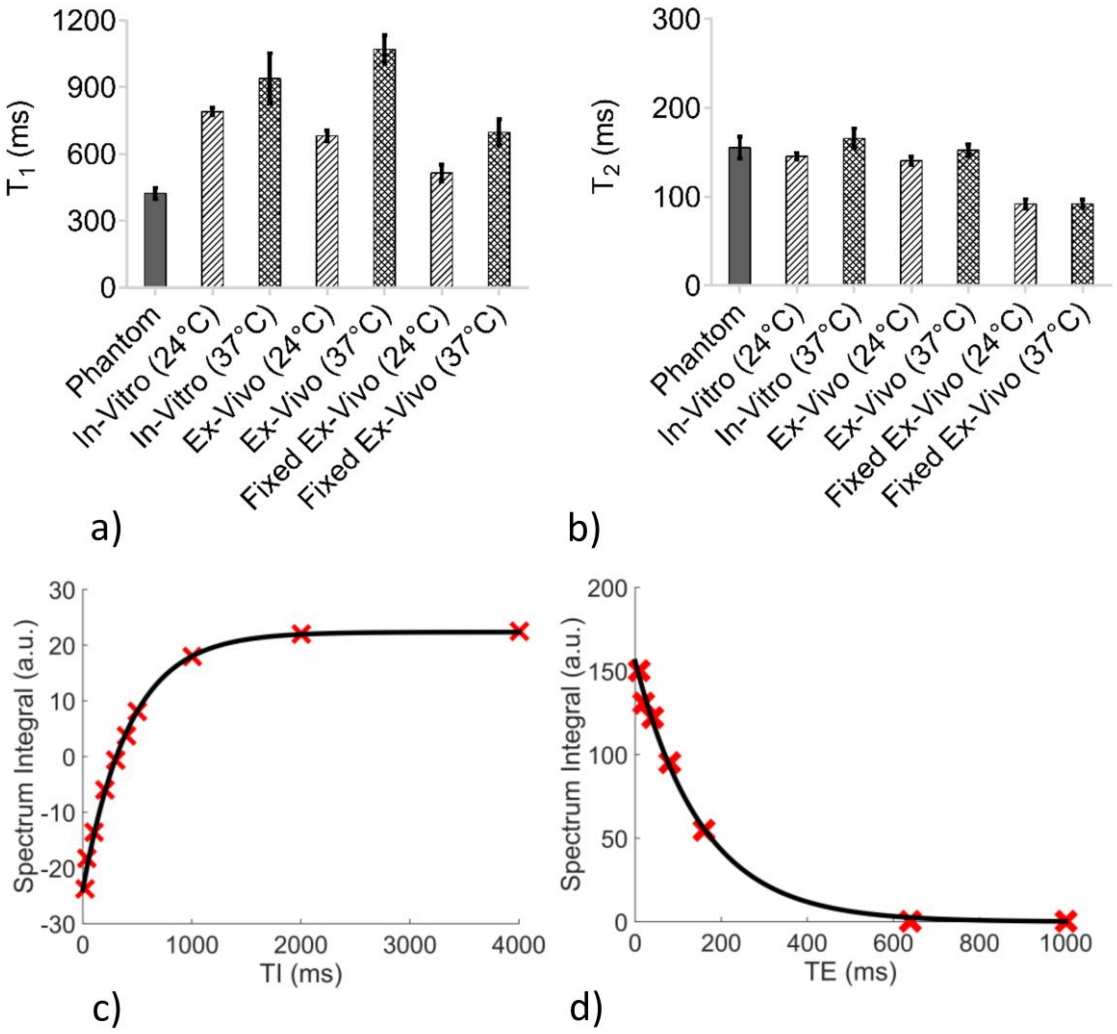

Figure 2: The effect of different cellular and temperature conditions on relaxation times. a-b) The T_1 and T_2 relaxation times of PFPE at different conditions. The relaxation times for the PFPE phantom were measured at 24°C. The T_1 relaxation time consistently increased in the cellular environments, and more so at the higher temperature. The T_2 relaxation time remained similar in all the conditions except the formaldehyde-fixed samples. Within the same cellular condition, the T_2 relaxation time increased as the temperature increased. Bars indicate the best fit value while the error bars indicate one standard deviation. **c-d)** Representative T_1 and T_2 fit curves for the PFPE phantom at room temperature. A high R^2 value (>0.99) for both relaxation curves confirmed the high fit quality.

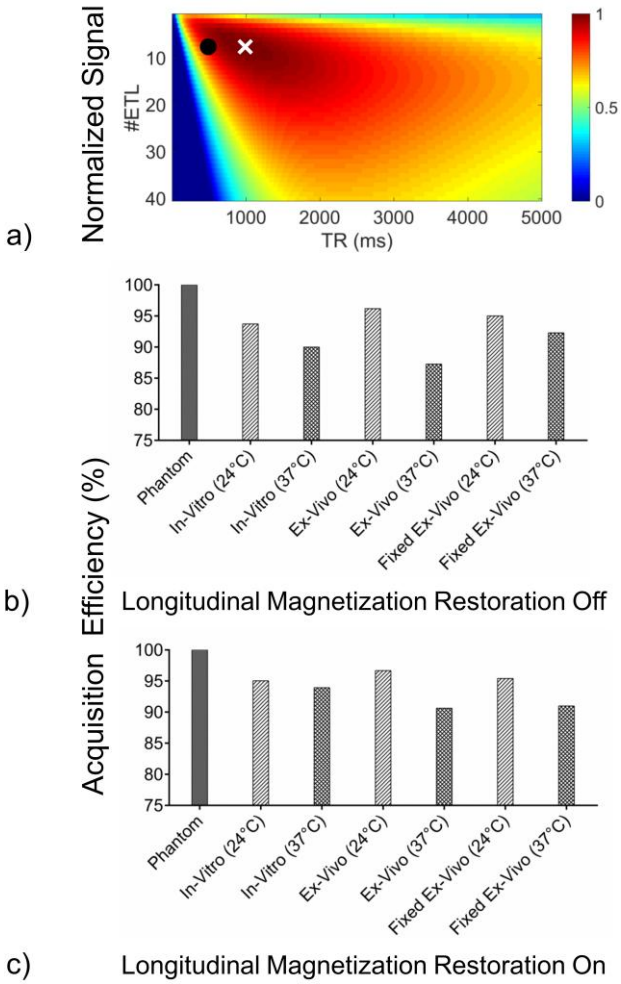

Figure 3: Pulse sequence optimization and acquisition efficiency. a) An example of the results of the Bloch equation simulations of the TSE optimization for a fixed bandwidth of 130 Hz/pixel, with the normalized signal as a function of ETL and TR, in this case for the ex-vivo PFPE sample at 37°C with LMR on. The white cross indicates the maximum normalized signal for this condition, while the black dot indicates the normalized signal at the TR and ETL obtained from the simulation for the reference phantom at 24°C. The ratio of the signals at these two parameter settings defines the acquisition efficiency η. **b)** Comparison of the relative acquisition efficiency η in the TSE pulse sequence with LMR off and **c)** LMR on for PFPE. With LMR off, the loss of η was small at room temperature (<6.5%), while it was moderate at body temperature (<13%). With LMR on, the loss of η was small at room temperature (<5.5%) and at body temperature (<10%).

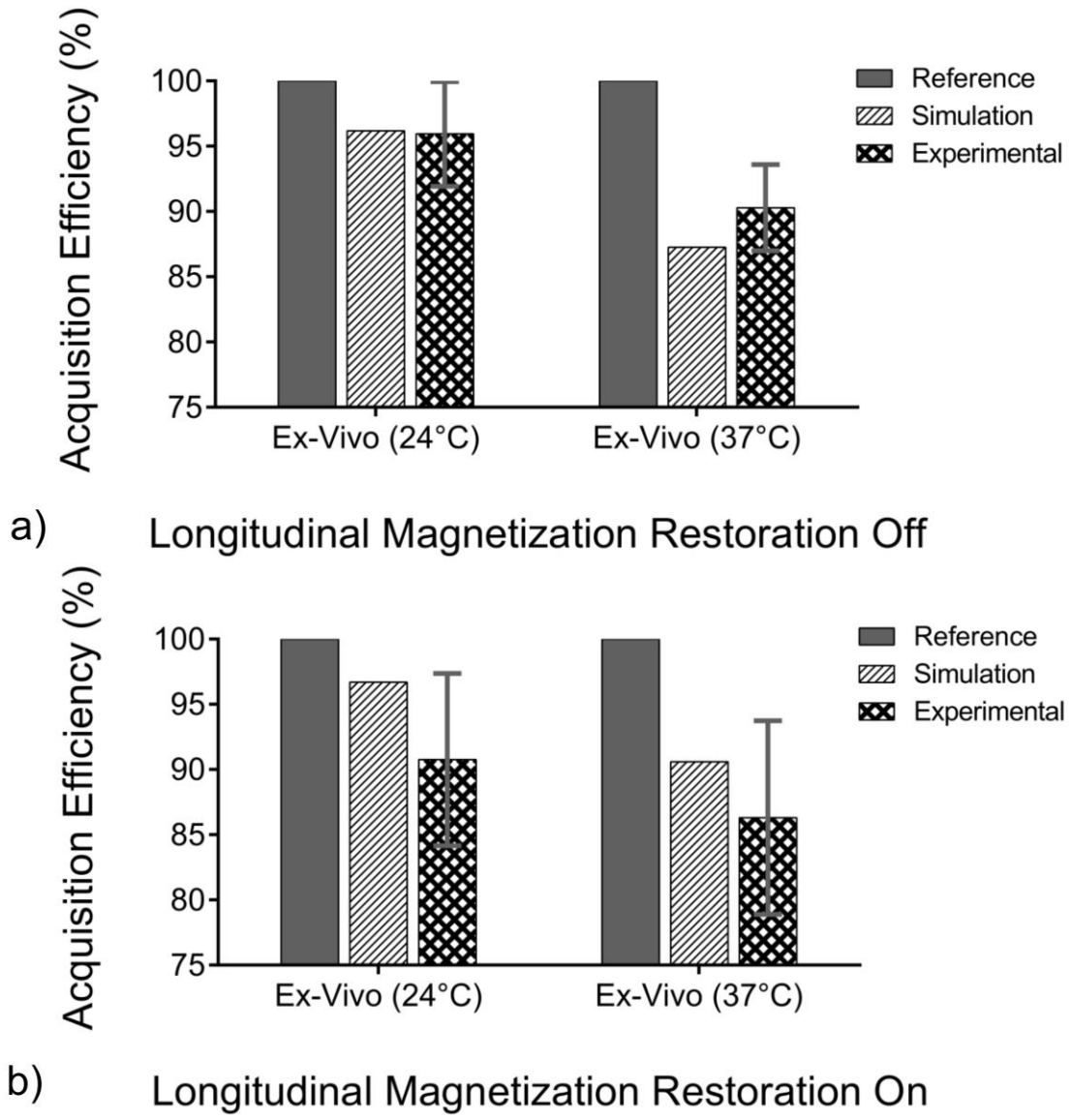

Figure 4: Experimental validation of the acquisition efficiency. a) The TSE pulse acquisition efficiency for the ex-vivo samples (i.e. the “ex-vivo cellular condition”) as compared to the reference at both 24°C and 37°C with the LMR pulse off and **b)** with the LMR pulse on. The results demonstrated a good agreement between the simulation and experiments.

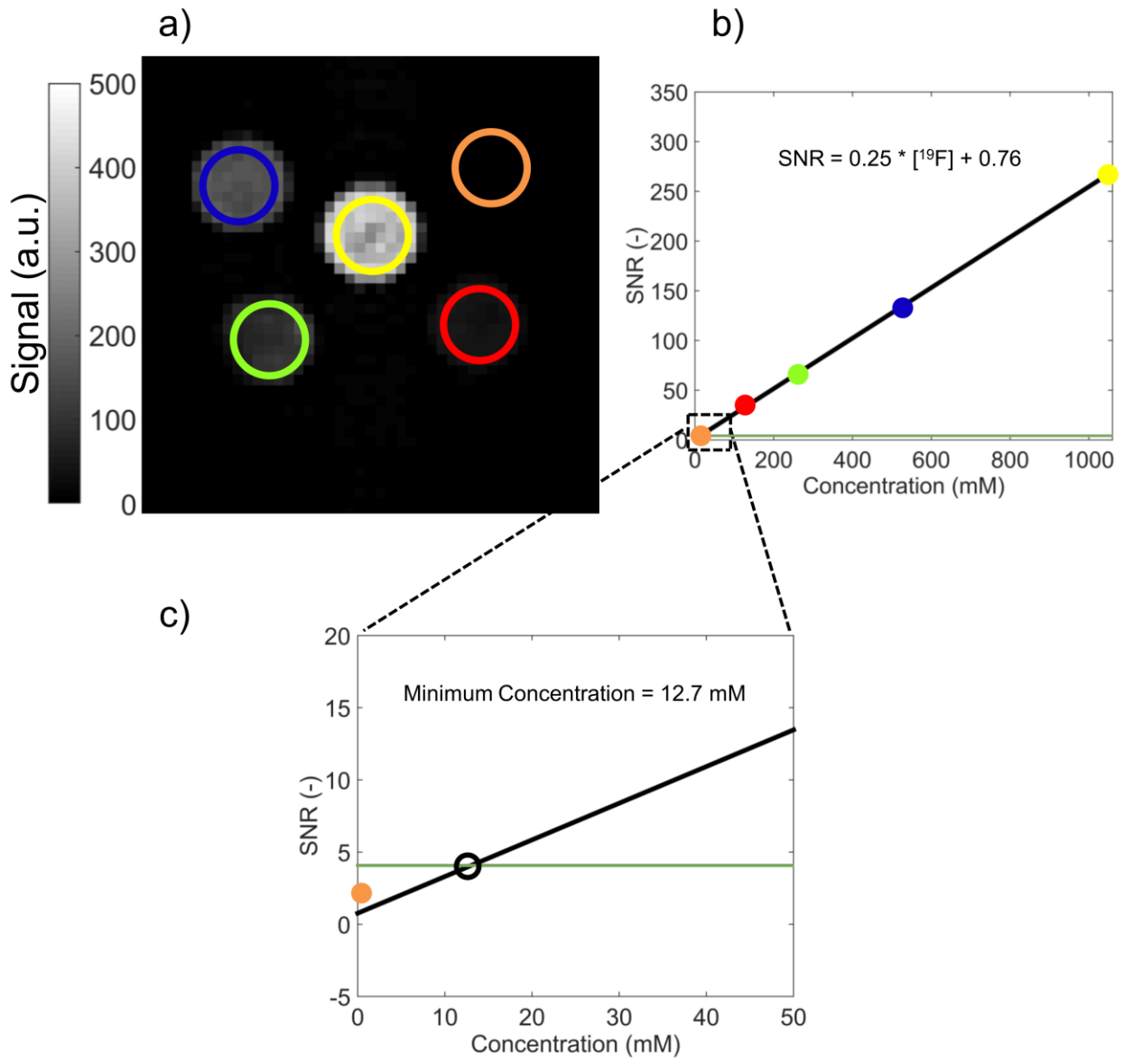

Figure 5: Illustration of the determination of the detection limit. a) An example of the drawn ROIs in a ^{19}F image of the PFPE phantom containing syringes with different ^{19}F concentrations. The locations of the syringes were established in ^{1}H images at the same location (not shown). **b)** An example of the linear curve fit of the calculated SNR versus ^{19}F concentration with matching color coding. **c)** The zoomed-in region shows the minimum detectable concentration (black circle), which was considered to be at SNR=4 (horizontal green line).